

Label Cleaning Multiple Instance Learning: Refining Coarse Annotations on Single Whole-Slide Images

Zhenzhen Wang, Aleksander S. Popel, Jeremias Sulam

Abstract—Annotating cancerous regions in whole-slide images (WSIs) of pathology samples plays a critical role in clinical diagnosis, biomedical research, and machine learning algorithms development. However, generating exhaustive and accurate annotations is labor-intensive, challenging, and costly. Drawing only coarse and approximate annotations is a much easier task, less costly, and it alleviates pathologists' workload. In this paper, we study the problem of refining these approximate annotations in digital pathology to obtain more accurate ones. Some previous works have explored obtaining machine learning models from these inaccurate annotations, but few of them tackle the refinement problem where the mislabeled regions should be explicitly identified and corrected, and all of them require a – often very large – number of training samples. We present a method, named Label Cleaning Multiple Instance Learning (LC-MIL), to refine coarse annotations on a *single* WSI without the need of external training data. Patches cropped from a WSI with inaccurate labels are processed jointly within a MIL framework, and a deep-attention mechanism is leveraged to discriminate mislabeled instances, mitigating their impact on the predictive model and refining the segmentation. Our experiments on a heterogeneous WSI set with breast cancer lymph node metastasis, liver cancer, and colorectal cancer samples show that LC-MIL significantly refines the coarse annotations, outperforming state-of-the-art alternatives, even while learning from a single slide. These results demonstrate that LC-MIL is a promising, lightweight tool to provide fine-grained annotations from coarsely annotated pathology sets.

Index Terms—Whole-slide image segmentation, multiple instance learning, coarse annotations, label cleaning.

I. INTRODUCTION

PATHOLOGY plays a critical role in modern medicine, and particularly in cancer care. Pathology examination and diagnosis on glass slides are the gold standard for cancer diagnosis and staging. In recent years, with advances in digital scanning technology, glass slides can be digitized and stored in digital form into whole-slide images (WSIs). These WSIs contain complete tissue sections and high-level morphological details, and are changing the workflow for pathologists [1], [2].

Diagnosis by pathologists on a WSI typically include the description of cancer (*i.e.*, presence, type, and grade of cancer),

This work was supported in part by CISCO research grant CG# 2686384, and NIH grants R01CA138264 and U01CA212007.

Z. Wang and J. Sulam (corresponding author) are with the Department of Biomedical Engineering, and the Mathematical Institute of Data Science, at Johns Hopkins University, MD 21218 USA (e-mail: {zwang218, jsulam1}@jhu.edu).

A. S. Popel is with the Department of Biomedical Engineering at Johns Hopkins University, MD 21218 USA (e-mail: apopel@jhu.edu).

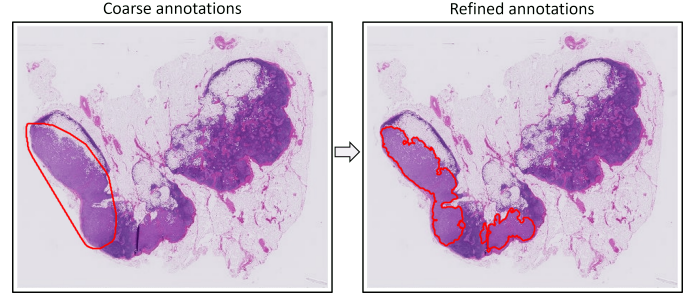


Fig. 1: Example of the refined breast cancer segmentation produced by our algorithm on a WSI of lymph node section, without requiring any external training data.

the estimation of tumor size, and observation of tumor margin (whether tumor cells appear at the edge of the tissue), which is important for planning therapy and estimating prognosis. Further information, such as the detailed localization of cancer, is usually not included in the routine pathology report. However, this local information on cancer is of great interest in biomedical and pharmaceutical research. The tumor microenvironment – the stromal tissue and blood vessels surrounding the tumor cell clusters – governs the tumor growth, response to treatment, and patient prognosis [3], [4]. The quantitative analysis of the tissue microenvironment, via downstream analysis of spatial statistics and other metrics, require the clear and accurate definition of the boundaries of the tumor, as in recent works [5]–[7].

On the other hand, the local detection and segmentation of histopathology images is a significant and rapidly growing field in computational pathology. Early approaches mainly focused on extracting the morphological and texture features using image processing algorithms [8], including thresholding [9], fuzzy c-means clustering [10], watershed algorithm [11], active contours [12], among others. With the advent of artificial intelligence and deep learning, a number of deep neural network models have achieved encouraging results in biomedical image segmentation [13], [14].

Whole-slide image segmentation, on the other hand, faces a unique challenge, since neural network models cannot be directly applied to the whole Gigapixel resolution WSI. The patch-based analysis (*i.e.*, training and deploying a model on numerous small patches that are cropped from the WSI) is commonly used as an alternative. Supervised deep learning has been remarkably successful on this patch-based WSIs analysis

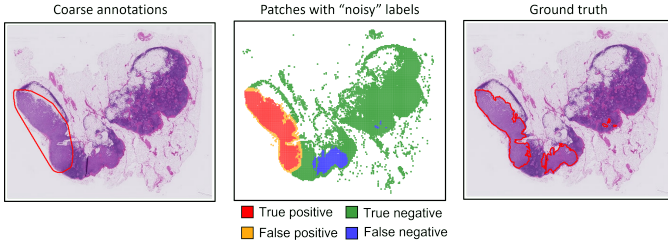


Fig. 2: Illustration of the “noisy” label problem in coarse annotations of WSI.

[15]. However, high quantity (and quality) of fine-grained annotations are needed, including patch-level or pixel-level information. The latter is very costly to obtain, since detailed manual annotation on Gigapixel WSIs is extremely labor-intensive and time-consuming, and suffers from inter- and intra-observer variability [16]–[18]. For these reasons, state-of-art WSI sets with detailed annotations provided by expert pathologists are very limited. The lack of large datasets with detailed and trustworthy labels is one of the biggest challenges in the development and deployment of classical supervised deep learning models in digital pathology applications.

Given the cost and difficulty of obtaining exhaustive and accurate annotations, a number of approaches attempt to address the segmentation problem in imperfect label settings [19]. Weakly-supervised learning aims to automatically infer patch-level (local) information using only slide-level (resp. global) labels, but it typically requires thousands of WSIs as training samples [20]–[22]. Semi-supervised learning, on the other hand, trains models on partially annotated WSI and makes predictions for the remaining unlabeled regions, yet the partial annotations must also be conducted by experts [23]. In this paper, we re-think the WSI annotation process from a more clinically applicable scenario: Drawing coarse annotations on WSIs (e.g., rough boundaries for the cancerous regions), is much easier than detailed annotations. Such coarse annotations need only similar effort and time as the slide-level labeling, and can even be conducted by non-experts. Learning from those coarse annotations, and then refining them with computational methods, might be an efficient way to enrich the labeled pathology data with minimal effort. The resulting refined annotation can provide a more accurate “draft” for the further detailed annotations by pathologists, and thus alleviate their workload.

Our solution to the coarse annotation refinement problem is based on a multiple instance learning (MIL) framework that intrinsically incorporates the fact that the input annotations are imperfect, models this imperfection as patch-level label noise, and finally outputs a refined version of annotations by identifying the mislabeled patches and correcting them, as Fig. 1 illustrates. Our methodology, named Label Cleaning Multiple Instance Learning (LC-MIL), is validated in a heterogeneous set of 120 WSIs from three cancer types, including breast cancer metastasis in lymph nodes, liver cancer, and colorectal cancer. Importantly, and in order to make our method applicable to scenarios where just a few cases (slides)

are available, our method can be trained and deployed on a single WSI, without the need for large training sets. Our approach significantly refines the original coarse annotations even while learning from a single WSI, and substantially outperforms state-of-the-art alternatives. To the best of our knowledge, this is the first time that multiple instance learning is employed to clean label noise, and ours is the first approach that allows for refining coarse annotations on single WSI.

The rest of the paper is organized as follows. In Section II we provide an overview of related work. In Section III, we present the proposed methodology, LC-MIL, as well as a state-of-art baseline method, in detail. We then proceed to out single-slide annotation refinement experiments in Section IV. Lastly, we discuss and summarize both the implication and limitations of our approach in Section V and Section VI.

II. RELATED WORK

In this section we discuss related work from the areas that are mostly related to our contribution: label noise handling and multiple instance learning in medical imaging.

Before we describe the specific techniques and studies, we first give a brief formulation of the problem to direct the reader to the appropriate context. The coarse annotations are considered as a “noisy” label problem. More specifically, a WSI consists of a number of small patches, each of which can be assigned a label based on the annotations: patches within the annotated cancerous regions are assigned positive labels, and otherwise negative labels are assigned. However, not all of the labels are correct, given that the annotations are inaccurate. Comparing the coarse annotations with the ground truth, we will find some false positives (yellow) and false negatives (blue), as Fig. 2 illustrates. Naturally, the model has no access to the ground truth, and aims at learning from, and modifying, the coarse annotations to retrieve the correct segmentation. This is the so-called “annotation refinement” problem, interpreted as identifying mislabeled samples and correcting their labels via machine learning approaches. This is a very challenging problem: the machine learning algorithm must be able to learn from inaccurate information and over considerable heterogeneity of tissue morphology and appearance, *and* do so without an external collection of training data.

A. Label noise handling

We place ourselves in a machine learning scenario, where we are given a collection of training data – pairs of samples and their corresponding labels, but part of training samples have their labels corrupted. The learning process, predicting a rule that assigns a label to a given sample, then become significantly more challenging.

Label noise handling is an extensively researched problem in machine learning. A large family of approaches focus on enhancing the robustness of a machine system against label noise by designing sophisticated model architectures [24]–[26], choosing loss functions that are tolerant to label noise [27]–[29], and conducting “label smoothing” [30]–[32]. This category of approaches typically does not evaluate the label accuracy or confidence of the training set, but tries to alleviate

the impact of the corrupted labels in the performance of the model in a held-out test set.

Some other approaches attempt to evaluate the label accuracy based on predicted probabilities [33]–[35] or loss values [36], [37], under the intuition that samples with less confident predictions or unusually high loss values are more likely to be mislabeled. However, probability and loss cannot reveal the prediction confidence correctly in many poorly-calibrated models [38]. An auxiliary set with clean labels –if available– is popular in label noise detection, which is either used as a reference to identify potentially mislabeled samples [39], [40], or re-weight the training samples to mitigate the impact of mislabeled samples on the system [41]–[43].

K-nearest neighbors (k-NN) based analysis [44], on the other hand, can be used for “editing” corrupted labels without an auxiliary clean set. The basic idea is to discard samples that are not consistent with their k nearest neighbors. In a recent work, k-NN has been deployed within deep learning frameworks, as the deep k-NN (DkNN) approach of [45], which searches for neighbors in the feature space of a deep learning model. This method outperformed the state of the art for label noise correction, and we will revisit it in further detail as we describe our baseline in Section III-B.

B. Multiple Instance Learning

Unlike supervised learning settings, where each training sample comes with an associated label, in multiple instance learning (MIL), one only has labels associated to groups of samples, $X_i = \{x_k\}_{k=1}^{n_i}$, termed *bags*, but not with the individual samples x_i , called *instances*. Although individual labels y_i exist for the instances x_i , they are unknown during training. However, the bag-level label Y_i is a function of the instance-level labels y_i . This function was simply a \max pooling operator when MIL was first proposed by Dietterich et al. [46], denoted as $Y = \max_i \{y_i\}$.

Over the years, various alternative MIL formulations were developed. Ilse et al. [47] provide a generalization of MIL predictors as a composition of individual functions:

$$P_{Y=1} = g(\sigma(f(X))). \quad (1)$$

Here, $f : \mathbb{R}^d \rightarrow \mathbb{H}$ is a transformation function mapping individual instances to a feature space or label space; $\sigma : (\mathbb{H})^k \rightarrow \mathbb{H}$ is a permutation invariant pooling function that aggregates the k transformed instances within a bag; and $g : \mathbb{H} \rightarrow \mathcal{Y}$ finally maps the aggregated instances to the corresponding bag label space.

When MIL is applied to medical imaging analysis, one typically considers an entire whole-slide image as a bag, and regards patches cropped from the corresponding slide as instances. The bag label depends on the presence (positive) or absence (negative) of disease in the entire slide. While often successful in bag label prediction, these approaches require very large datasets with thousands of slides [20]–[22]. Moreover, the disease localization, or instance-level predictions, usually suffers from the lack of supervision and underperforms the fully supervised counterparts [48], [49]. Moreover, local detection is usually considered as an additional – sometimes

optional – task instead of the primary goal in MIL studies. Even if a heatmap or a saliency map is generated to highlight the diagnostically significant regions, the localization performance is not always quantitatively validated [20], [21], [50].

Some works integrate other forms of weak annotations to the MIL framework to boost the local detection performance. CDWS-MIL, proposed by [51], introduced the percentage of the cancerous region within each image as an additional constraint to improve disease localization compared with using image-level labels only. CAMEL, proposed by [52], first splits the WSI into latticed patches, and considers each patch as a bag. A MIL model is then used to generate a pixel-wise heatmap for each patch. Those weak annotations, although easier to obtain than pixel-wise annotations, still need substantial effort and domain expertise. Our proposed method, on the other hand, is able to manage very coarse annotations, which are much easier to obtain, even without domain expertise.

III. METHODS

In this section, we first formulate the problem at hand and then proceed to describe the baseline method, DkNN, and our proposed approach, label cleaning multiple instance learning (LC-MIL), respectively.

A. Problem formulation

We consider a single whole-slide image (WSI) with some coarse annotations for regions of interest (e.g., cancerous regions) as a dataset with noisy labels. The WSI is latticed to generate N square patches, denoted as $\mathbb{S} = \{(x_i, y_i)\}_{i=1}^N$. Each patch $x_i \in \mathbb{R}^d$ is assigned a label $y_i \in \{0, 1\}$ based on the coarse annotations provided. To be more specific, a patch is assigned a positive label if it falls within the positively annotated area (e.g., cancerous region), and negative otherwise, as Figure 3 illustrates. In a practical setting, there may be some patches at the intersections of two classes of regions. For those patches, the assigned labels are decided by the location of patch centers. In other words, as soon as the center of a patch falls into positively annotated regions, a positive label is assigned, and negative otherwise.

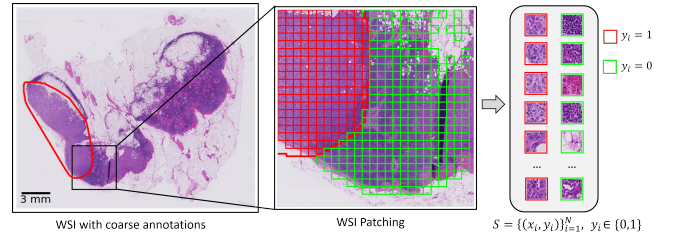


Fig. 3: WSI patching and patch-level noisy labels assignment.

Importantly, we do not assume that all patches in the positively annotated area are actually positive: since the coarse annotations cannot delineate the disease regions precisely, there must be patches having an incorrect label assigned to them. Similarly, not all patches in the negative annotated area are true negatives, implying that there might be “missed positive regions”. The problem of refining this coarse (and

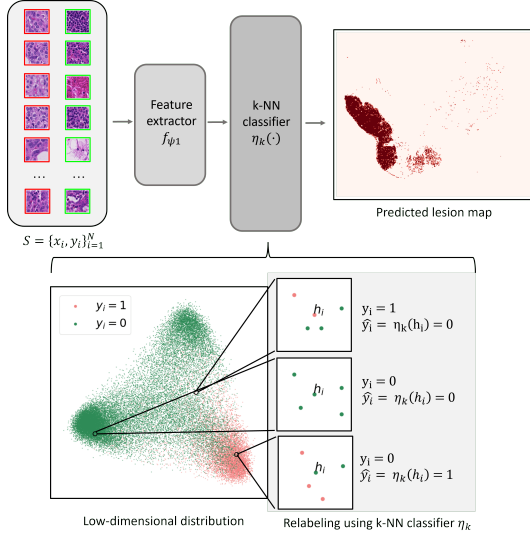


Fig. 4: **Overview of DkNN (baseline) framework.** Patches are first mapped to the low-dimensional feature space using feature extractor f_{ψ_1} , and then relabeled by the k-NN classifier η_k .

inaccurate) annotation can then be interpreted as detecting the mislabeled patches.

B. Our baseline

It should be noted that, to the best of our knowledge, the problem of learning a segmentation algorithm for WSI data from a single slide with inaccurate annotations has never been studied before. As a result, there are no available methods that can be deployed in an off-the-shelf manner. Thus, to provide a baseline for our problem, we employ a state-of-the-art algorithm that can correct label noise without an auxiliary clean set, while at the same time being able to employ data-driven (learnable) feature extractors that are crucial for learning discriminative representations from WSIs.

The k-nearest neighbors (DkNN) algorithm has been popular for “editing” corrupted labels since it was first proposed by Wilson in 1972 [44]. Here, we use a recently proposed deep k-nearest neighborhood (k-NN) model [45] as our baseline, which has demonstrated state-of-the-art results in the label cleaning problem. The framework is illustrated in Figure 4.

In this DkNN algorithm, the noisy-labeled samples, x_i , are mapped to a feature space $\mathbb{H} \subset \mathbb{R}^m$, so that $h_i = f_{\psi_1}(x_i)$, using a feature extractor $f_{\psi_1} : \mathbb{R}^d \rightarrow \mathbb{R}^m$, parameterized by a deep neural network. The parameters of f_{ψ_1} are fit by training a binary classifier \mathbb{C} on the noisy-labeled samples in an end-to-end manner, as we detail later. All instances are then re-labeled using a k-NN classifier η_k via majority voting. More precisely, the predicted label for instance x_i can be denoted as:

$$\hat{y}_i = \eta_k(h_i). \quad (2)$$

In this way, the labels for instances x_i are re-assigned: if a positive instance is surrounded mostly by positive instances in feature space, this label is likely correct. If it is not, however, the label is likely incorrect and therefore changed. In other

words, the re-assigned label of each instance is decided by majority voting among its k nearest neighbors in feature space. Finally, a binary map is then generated from those predicted labels \hat{y}_i of corresponding patches.

The definition of a k-nearest neighbor classifier, η_k , is by now standard, but we include it here for completeness. Denoting by H the set of computed features, $H = \{h_i\}$, let the k-NN radius for a given feature $h_i \in \mathbb{H}$ be $r_k(h_i) := \inf\{r : |B(h_i, r) \cap H| \geq k\}$, where $B(h_i, r) := \{h_j \in H : \|h_i - h_j\|_2 \leq r\}$ is the ball of radius r and centered at h_i . The k nearest neighbors of h_i are given by $N_k(h_i) := B(h_i, r_k(h_i)) \cap H$. The k-NN classifier for any $h_i \in \mathbb{H}$ can then be denoted as

$$\eta_k(h_i) := \operatorname{argmax}_{y=\{0,1\}} \sum_{j=1}^{|N_k(h_i)|} 1[y_j = y, h_j \in N_k(h_i)].$$

Finally, it remains to specify the feature extractor f_{ψ_1} . To learn reasonable and discriminant representations for patches, we built a binary classifier \mathbb{C} on the basis of the feature extractor f_{ψ_1} by attaching a fully connected layer (FCN) and a Sigmoid layer. The end-to-end classifier $\mathbb{C} \circ f_{\psi_1}$ is trained on the noisy dataset $\mathbb{S} = \{(x_i, y_i)\}_{i=1}^N$ in a fully supervised manner, and using a cross-entropy loss. After training concludes, we discard the classifier \mathbb{C} and use f_{ψ_1} within the k-NN algorithm, as described above.

C. Label Cleaning MIL (LC-MIL)

Our proposed methodology, Label Cleaning Multiple Instance Learning (LC-MIL), tackles the noisy label problem from a MIL framework. Broadly speaking, our approach consists on a multiple instance learning model – implemented via a deep attention mechanism [47] – that is trained to classify *bags* of patches from a single WSI image with noisy labels. Once this model is trained, it is then employed to re-classify all patches in the image by constructing singleton bags. The corresponding predictions are used to correct the original noisy labels, and in doing so, refining the inaccurate segmentation. Fig. 5 depicts an overview of our LC-MIL algorithm, and we now expand on the details of each component.

MIL dataset construction: As briefly mentioned above, in order to give our approach maximal flexibility in terms of the availability of training data, we situate ourselves in the case of having a single WSI, which represents all the data available to the algorithm – we will comment on extensions to cases with access to larger datasets later.

From a single WSI, we construct our noisy dataset of image patches $\mathbb{S} = \{(x_i, y_i)\}_{i=1}^N$, comprising positive and negative cases: (1) $\mathbb{S}_P := \{(x_i, y_i) \in \mathbb{S} : y_i = 1\}$, which consists of all of the patches with a positive label; (2) $\mathbb{S}_N := \{(x_i, y_i) \in \mathbb{S} : y_i = 0\}$, which consists of all of the patches with a negative label. In our context, where labels are determined by only coarse and inaccurate annotations, there are likely false positives in \mathbb{S}_P and false negatives in \mathbb{S}_N . However, we assume that the majority of the labels in both subsets are correct. With this assumption, we construct a positive bag X_j by selecting (uniformly at random) n_j instances from \mathbb{S}_P , and construct a negative bag analogously with instances from \mathbb{S}_N . We are

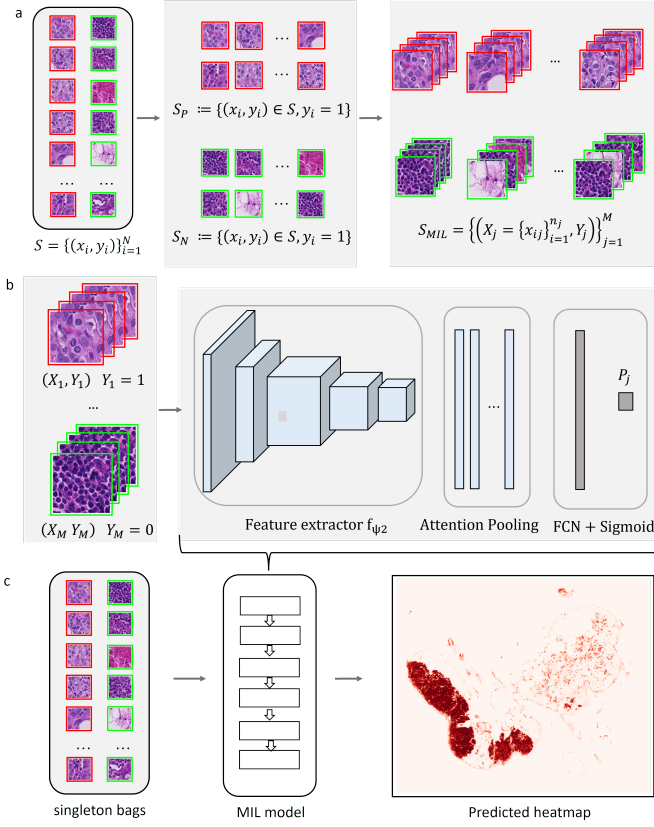


Fig. 5: **Overview of the LC-MIL framework.** (a) MIL dataset construction: patches in WSI are split into two subsets \mathbb{S}_P and \mathbb{S}_N based on the original coarse annotations. (b) An attention based MIL model is trained on bags $X_i = \{x_{ij}\}_{j=1}^{n_i}$. (c) At inference, each patch is considered as a singleton bag and receives risk score to generate a predicted heatmap.

able to create virtually as many bags as desired from one single WSI, since the sampling is conducted with replacement. The constructed MIL dataset with M bags can be defined as:

$$S_{MIL} = \{(X_j = \{x_{ij}\}_{i=1}^{n_j}, Y_j)\}_{j=1}^M, \quad (3)$$

where x_{ij} is the i th instance in X_j , and Y_j refers to the bag-level label, given by

$$Y_j = \begin{cases} 1, & \text{if } X_j \subset \mathbb{S}_P \\ 0, & \text{if } X_j \subset \mathbb{S}_N. \end{cases} \quad (4)$$

Note that n_j , the number of instances within a bag, need not be constant, and the detailed setting can be found in Supplementary Section I.

Architecture and Training: We built a deep MIL model to predict the bag-level score P_j , under the composite function framework as described in Section II-B and Eq. (1). We detail the three functions below:

- 1) A feature extractor, parameterized by a deep neural network f_{ψ_2} , is used to map the instance x_{ij} to a low-dimensional embedding, denoted as:

$$h_{ij} = f_{\psi_2}(x_{ij}). \quad (5)$$

- 2) An attention-based MIL pooling operator σ , which gives each instance a weight w_{ij} and aggregates the low-dimensional embeddings of all instances using a weighted average to generate a representation for the whole bag. Importantly, these weights are learnable functions of the features, too. More specifically, we have that:

$$z_j = \sigma(\{h_{ij}\}_{i=1}^{n_j}) = \sum_{j=1}^{n_j} w_{ij} h_{ij}, \quad (6)$$

with weights given by

$$w_{ij} = \frac{\exp\{W \tanh(V h_{ij})\}}{\sum_{k=1}^{n_j} \exp\{W \tanh(V h_{ik})\}}. \quad (7)$$

Here, both W and V are learnable parameters.

- 3) A linear classifier g , which predicts the bag label based on the computed representation, z_i . The predicted score, P_i , is finally obtained by the appropriate logistic function, defined as:

$$P_j = g(z_j) = \frac{1}{1 + e^{-\langle g, z_j \rangle}}, \quad (8)$$

where g is a learnable vector.

Unlike [47], who employ a cross-entropy loss, we use the focal loss [53] in order to promote better calibration of the predicted probabilities. This loss is defined as:

$$L = -(Y_j(1 - P_j)^\gamma \log P_j + (1 - Y_j)P_j^\gamma \log(1 - P_j)), \quad (9)$$

where γ is a user-specified parameter, and the reader can check our setting in Supplementary Section I.

Inference: There is typically a “gap” between bag-level and instance-level prediction in MIL approaches, where the instance-level score is not directly predicted by the model. Although the attention pooling operator provides a way to locate key instances, those weights cannot be interpreted as instance-level scores directly. Here, we propose to use “singleton bags” as a simple solution, enabling us to exploit the (calibrated) scores provided by the classification model: for bags consisting of only one instance, the bag-level prediction is equal to the instance-level prediction. In this way, during the inference phase, we revisit the noisy dataset $\mathbb{S} = \{(x_i, y_i)\}_{i=1}^N$ using the trained MIL model. Instead of randomly choosing a subset of instances to pack a bag, as done during training, every single instance x_i is now considered as a “single-instance bag”. Since there is only one instance in a bag, the attention-based pooling in the MIL framework has no impact during inference and the predicted score for each instance can be denoted as:

$$\hat{p}_i = \frac{1}{1 + e^{-\langle g, f_{\psi_2}(x_i) \rangle}}. \quad (10)$$

A predicted heatmap is then generated based on these likelihoods, where the value of each pixel refers to the risk score $p_i \in [0, 1]$ of the corresponding patch in the WSI.

In addition to the central machine learning component of our method, detailed above, our experiments involve other implementations details, which we detail in Supplementary Section I. All software implementations of our methods are publicly available¹.

¹Available at <https://github.com/Sulam-Group/MIL-pathology>

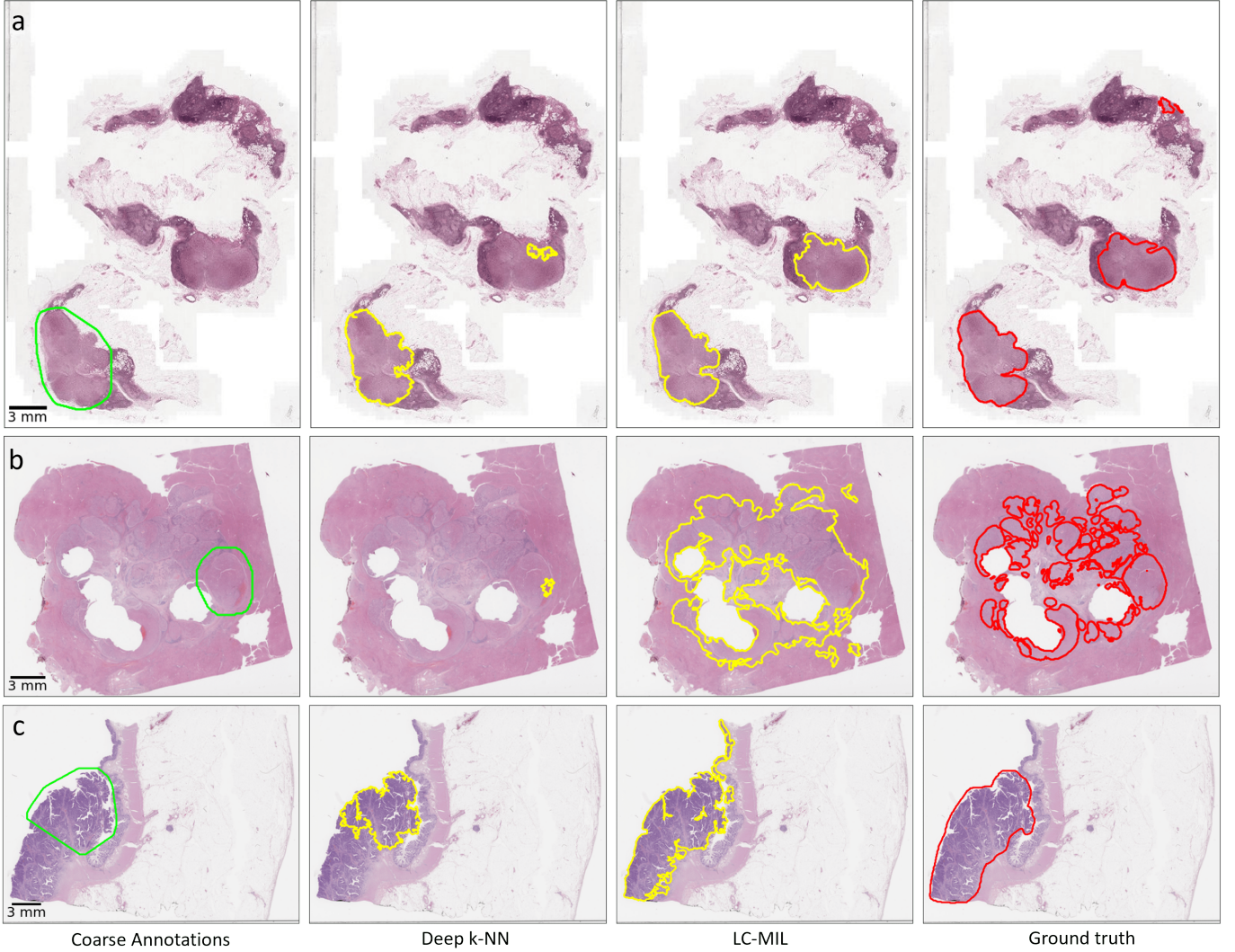


Fig. 6: **Examples of simulated coarse annotations and refinement.** For (a) CAMELYON16, (b) PAIP2019, and (c) PAIP2020, one WSIs from each subset was shown. From left to right, four versions (coarse annotations (1st column, lime lines); coarse annotations (2nd column, yellow lines); predicted contours using DkNN (3rd column, yellow lines); predicted contours using LC-MIL (4th column, red lines)) of cancerous regions contours are shown.

IV. EXPERIMENTS

In this section, we first describe our dataset and implementation details, and then show two coarse annotation refinement scenarios in simulated and real-world settings, separately.

A. Dataset

We evaluated the coarse annotation refinement performance on three publicly available histopathology datasets. These datasets were chosen because they include different tissues and degrees of morphological heterogeneity, but also because of the availability of expert annotations that will be regarded as ground-truth for the quantitative evaluation of our method.

- 1) CAMELYON16 [54]: contains a total of 399 hematoxylin and eosin (H&E) stained WSIs of lymph node sections from breast cancer patients. Detailed hand-drawn contours for metastases are provided by expert pathologists.

- 2) PAIP2019 [55]: contains a total of 100 H&E stained WSIs of liver cancer resection samples. The boundary of viable tumor nests was annotated precisely by expert pathologists. The viable tumor nests annotations are available for 60 WSIs.
- 3) PAIP2020²: contains a total of 118 H&E stained WSIs of colorectal cancer resection samples. The contours of the whole tumor area, which is defined as boundary enclosing dispersed viable tumor cell nests, necrosis, and peri- and intratumoral stromal tissues, are provided by expert pathologists. The whole tumor annotations are available for 47 WSIs.

²De-identified pathology images and annotations used in this research were prepared and provided by the Seoul National University Hospital by a grant of the Korea Health Technology R&D Project through the Korea Health Industry Development Institute (KHIDI), funded by the Ministry of Health&Welfare, Republic of Korea (grant number: HI18C0316).

TABLE I: Summary of refinement on simulated coarse annotations

Dataset	Num	Method	Accuracy	TPR	PPV	F1	Cleaned (%) ²	Mis-modified (%) ³
CAMELYON16	24	CA ¹	0.835 \pm 0.071	0.604 \pm 0.230	0.672 \pm 0.134	0.610 \pm 0.156	—	—
		DkNN	0.864 \pm 0.080	0.532 \pm 0.291	0.813 \pm 0.259	0.605 \pm 0.268	34.4 \pm 18.9	2.3 \pm 2.6
		LC-MIL	0.930 \pm 0.048	0.875 \pm 0.100	0.862 \pm 0.150	0.853 \pm 0.092	75.8 \pm 11.1	3.8 \pm 3.9
PAIP2019	54	CA	0.834 \pm 0.106	0.758 \pm 0.265	0.746 \pm 0.118	0.726 \pm 0.180	—	—
		DkNN	0.854 \pm 0.110	0.742 \pm 0.308	0.789 \pm 0.185	0.729 \pm 0.244	25.2 \pm 16.6	1.4 \pm 1.7
		LC-MIL	0.889 \pm 0.082	0.899 \pm 0.129	0.824 \pm 0.189	0.836 \pm 0.134	70.6 \pm 20.2	6.4 \pm 5.4
PAIP2020	42	CA	0.750 \pm 0.097	0.497 \pm 0.080	0.836 \pm 0.086	0.619 \pm 0.079	—	—
		DkNN	0.732 \pm 0.106	0.410 \pm 0.113	0.886 \pm 0.087	0.550 \pm 0.118	9.3 \pm 4.0	5.5 \pm 3.7
		LC-MIL	0.811 \pm 0.112	0.745 \pm 0.201	0.825 \pm 0.134	0.754 \pm 0.121	60.8 \pm 22.5	10.7 \pm 5.3

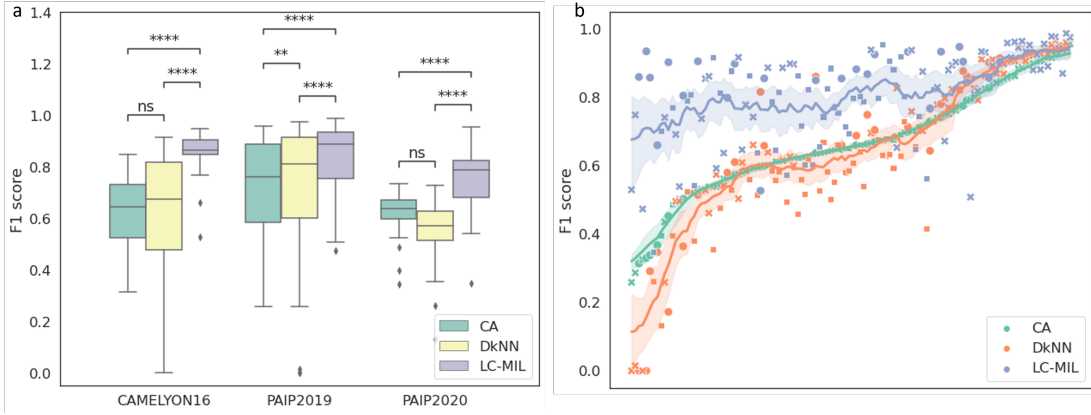
¹ Coarse annotations;² The ratio between cleaned samples and all mislabeled samples in original coarse annotations;³ The ratio between mis-modified samples and all correctly labeled samples in original coarse annotations.

Fig. 7: **Overview of refinement on simulated coarse annotations (F1 score).** (a) Boxplots of F1 scores of three versions of annotations. (*), (**), (***) and (****) denote p value of (0.01, 0.05], (10^{-3} , 10^{-2}], (10^{-4} , 10^{-3}] and (0, 10^{-4}], respectively, for the test that the median of difference between two observations is zero. (b) Refinement performance (F1 score) in different label noise conditions, slides sorted by the F1 scores of coarse annotations. The original metrics (\bullet (CAMELYON16), \blacksquare (PAIP2019), $*$ (PAIP2020)), the moving average (solid lines), where window size $k = 15$, and the 95% confidence interval for k observations (shaded areas) are shown.

The experimental design had the goal of validating the segmentation refinement, capability of our method on every single slide independently, and thus slides with almost all regions of a single class (cancer or normal) were excluded to ensure that our model had sufficient positive and negative samples. We set an upper bound of 90% and a lower bound of 10% for the ratio of lesion area as the data inclusion criteria. Slides marked with “not exhaustively annotated” were also excluded. A total of 120 slides (CAMELYON16: 24; PAIP2019: 54; PAIP2020: 42) were included, as shown in Supplementary Fig. 1.

B. Simulated coarse annotations

For each of the WSIs, we considered the annotations provided by expert pathologists as the ground truth. To simulate the clinical context of noisy annotations on WSI, we generated coarse annotations automatically via a custom procedure, as described in Supplementary Section I. Our method, LC-MIL, was robust to the choice of how to obtain these coarse annotations, and the employed procedure had the purpose of simulating both false positives as well as false negatives in the initial inaccurate annotation, and Fig. 6 presents a few of the simulated coarse annotations on its left-most column.

The proposed method (LC-MIL) and our baseline (DkNN) were applied to each WSI independently to refine the coarse annotations. Fig. 6 shows a few examples of the refinement performance, and the reader can find more examples in Supplementary Fig. 2. The evaluation is also conducted on each slide independently. For each slide, we calculated the accuracy, precision (PPV), sensitivity (TPR), and F1 score for three versions of annotations: (1) initial coarse annotations, (2) predicted annotations by DkNN, and (3) predicted annotations by LC-MIL. Note that we conduct a patch-based evaluation for the lesion localization results, where a true positive (TP) is defined as a detected cancerous patch that is actually cancerous as per the expert annotations.

We summarise the quantitative results of refinement on simulated coarse annotations in Table I. Particularly, we show the boxplots as well as the statistical comparison of three versions of annotations using a pairwise Wilcoxon signed-rank test [56] in Fig. 7 (a). To evaluate the refinement performance under different label noise conditions, we sorted the coarse annotations according to their F1 score, and then plot F1 scores of three versions of annotations, as shown in Fig. 7 (b). The same analysis was also conducted for accuracy, which can be found in Supplementary Fig. 4.

Overall Performance: The proposed method, LC-MIL, sig-

nificantly improves disease localization of coarse annotations and corrects incorrect labels, and substantially outperforms the baseline method, DkNN. After applying LC-MIL, over 60% of the mislabeled patches are identified and corrected, while less than 10% of the original correctly labeled patches are mis-modified (Table I). The average accuracy and F1 score are significantly improved. On the other hand, the refinement of DkNN is less efficient. Only about 30% (especially, less than 10% in PAIP2020) of the mislabeled patches are fixed by this method. In some cases, DkNN fails to bring significant improvement (*e.g.*, F1 score in CAMELYON16), and even gets lower metric values (*e.g.*, accuracy and F1 score in PAIP2019), which illustrates the difficulty of the learning problem under consideration.

LC-MIL is especially useful in detecting missed lesions. If we focus on two columns (*i.e.*, PPV and TPR) in Table I, we will find that both DkNN and LC-MIL can efficiently improve PPV (*i.e.*, making tumor boundaries more precise), but LC-MIL shows obvious advantages in improving TPR (*i.e.*, detecting missed lesions). Fig. 6 (b) is also a representative example of the exceptional ability to detect missed lesions of LC-MIL.

Refinement shows some heterogeneity in different coarse annotation conditions (Fig. 7 (b)). When the original coarse annotations are poor (*e.g.*, F1 scores of coarse annotations lower than 0.6), DkNN fails to bring any refinement and obtains even lower F1 scores in most cases, while LC-MIL manages to get F1 scores around 0.7. When the F1 score of coarse annotations falls between 0.6 – 0.8, DkNN manages to obtain a slightly higher F1 score but the improvement is not consistent, while LC-MIL continues to obtain F1 scores around 0.8. When coarse annotations are substantially good (*e.g.*, F1 score of coarse annotations higher than 0.8), both DkNN and LC-MIL achieve slightly higher F1 scores.

C. Real-world test: annotation with untrained eyes

To evaluate the annotation refinement performance in a real-world scenario, we recruited 29 untrained volunteers to annotate the WSIs: graduate students of biomedical engineering but with no obvious connection to digital pathology. The 29 annotators were distributed among the three datasets proportional to the dataset size (CAMELYON16:6, PAIP2019:13, PAIP2020:10). Each of them was asked to learn about the cancer morphology from two “learning samples” (2 WSIs with ground truth provided), and then to annotate another 15-16 WSIs. Overall, 441 versions of coarse annotations were collected, and each WSI was annotated by 3-5 different annotators. Similar to the simulated scenario, the refinement was also conducted with both methods, and evaluated on each slide with a specific version of coarse annotations independently.

Heterogeneity and validity of the manual annotations: Unlike the fully controllable simulated scenario, where all coarse annotations are automatically generated by a custom algorithm, hand-drawn annotations by untrained volunteers show more heterogeneity in quality and styles. Supplementary Fig. 3 shows some typical annotations and the refinement results that reflect this great difference between annotators. This

large heterogeneity includes cases that violate our working assumptions: the majority of positively annotated patches are TP, and the majority of negatively annotated patches are TN, which can be re-formulated as:

$$PPV > 0.5, NPV > 0.5. \quad (11)$$

We therefore split the coarse annotations into two groups based on this criterion (Eq. 11), and report the refinement results separately as “valid” or “not valid“, as Table II shows. The majority (about 85%) of hand-drawn annotations are valid according to our criteria (*i.e.*, satisfying Eq. 11). Noticeably, the F1 scores of these annotations have already reached around 0.85. After applying LC-MIL, the F1 scores are further improved to nearly 0.9 in lymph node metastasis (CAMELYON16) and liver cancer (PAIP2020) samples.

TABLE II: Summary of refinement on hand-drawn coarse annotations

Dataset	Valid	Method	Accuracy	F1
CAMELYON16	no 14.13%	CA	0.773 ± 0.091	0.519 ± 0.103
		DkNN	0.866 ± 0.105	0.683 ± 0.132
		LC-MIL	0.904 ± 0.064	0.736 ± 0.091
	yes 85.87%	CA	0.907 ± 0.066	0.839 ± 0.080
		DkNN	0.935 ± 0.055	0.885 ± 0.064
		LC-MIL	0.943 ± 0.043	0.891 ± 0.056
PAIP 2019	no 18.88 %	CA	0.573 ± 0.208	0.369 ± 0.205
		DkNN	0.580 ± 0.230	0.354 ± 0.242
		LC-MIL	0.575 ± 0.239	0.393 ± 0.240
	yes 81.12 %	CA	0.899 ± 0.074	0.860 ± 0.100
		DkNN	0.915 ± 0.073	0.881 ± 0.105
		LC-MIL	0.929 ± 0.061	0.899 ± 0.088
PAIP 2020	no 15.03 %	CA	0.568 ± 0.164	0.534 ± 0.160
		DkNN	0.576 ± 0.177	0.539 ± 0.187
		LC-MIL	0.598 ± 0.181	0.545 ± 0.188
	yes 84.97 %	CA	0.878 ± 0.086	0.843 ± 0.127
		DkNN	0.886 ± 0.090	0.851 ± 0.141
		LC-MIL	0.846 ± 0.071	0.804 ± 0.104

Colorectal cancer exhibits confounding morphology. In the case of (PAIP2020), where the original coarse annotations have F1 scores around 0.84, and DkNN improves it slightly (0.85), but LC-MIL gets a lower F1 score (0.80), caused by the heterogeneity and complexity of colon histology. Colorectal tissue samples typically contain epithelial tissues, where the cancer begins developing, loose connective tissue and smooth muscles. The differences between epithelial and other tissues are much more significant than the contrast between benign and malignant epithelial tissues, so that the LC-MIL model is misled to discriminate epithelial tissues from any other regions, and that is why some normal epithelial tissues get false positive detection (see Fig. 6 (c) as an example).

V. DISCUSSION

The main hypothesis addressed in this work is that the coarse annotations on the whole-slide images (WSIs) can be refined automatically even from very limited data. This problem had remained unstudied until now due to the technical challenges that often make deep learning models require very large training sets, and could alleviate the workload of expert pathologists.

To test our hypothesis, we developed the Label Cleaning Multiple Instance Learning (LC-MIL) method to refine

the coarse annotations. Our experiments on a heterogeneous dataset with 120 WSIs across three different types of cancers show that LC-MIL can be used to generate a significantly better version of disease segmentation, even while learning from a single WSI with very coarse annotations. The unsatisfying performance of DkNN, a state-of-the-art method for label noise cleaning, highlights the difficulty of the learning problem we are tackling in this work.

Our methodology has implications in both engineering and clinical domains. From a machine learning perspective, LC-MIL demonstrates the potential of the MIL framework to be used in a label cleaning context. Our setting can be considered as a significant complement to existing label cleaning methods, without requiring the need for an auxiliary clean set of samples. From a clinical perspective, the proposed methodology could be used to alleviate pathologists' workload in annotation tasks. LC-MIL allows pathologists to draw coarse annotations quickly and obtain a refined version for reference. On the other hand, our results show that the refinement produced by LC-MIL is especially significant when the coarse annotations are very inaccurate, which implies that the proposed methodology could be useful for helping those very inexperienced annotators. Importantly, our approach is particularly useful for increasing TPR, therefore detecting tumor areas that might have been missed by an inexperienced, or distracted, annotator.

A significant advantage of the LC-MIL is its ability to work in extreme data-scarcity scenarios, as it can be deployed on a single WSI. We have chosen to study this setting to showcase the flexibility of our approach. However, this also constrains the minimal and maximal ratio of cancerous regions if the refinement is conducted per slide, since a minimal amount of both negative and positive samples within one slide are needed for the learning algorithm. This limitation could be addressed by moving beyond the *single* WSI case and aggregating patches from multiple slides during the learning phase, if such data is available. Moving from this single-slide to the multiple-slide settings is a natural extension of our methodology, which we will explore in future work.

Another limitation of LC-MIL, probably also shared by other binary classifiers, is that the model can be confused by irrelevant information when the histology structure is complex and heterogeneous. An example of this is that the LC-MIL model tends to be misled to discriminate epithelial tissues from other types of tissues (loose connective tissue, smooth muscle), instead of focusing on learning the difference between benign and malignant tissue. On the other hand, it may not be challenging for human eye, even for non-experts, to eliminate the interference of other tissue types. We suggest that this can be addressed by extending the current version of LC-MIL to a multi-class setting. We also leave it as future work.

An important open question remains: can detailed annotations by experts be replaced by simple coarse annotations, with the help of our methodology? The average obtained F1 scores reside around 0.85 for lymph node metastasis samples (and slightly lower for others), starting with the simulated coarse annotations. In the real-world test, where untrained volunteers make annotations and LC-MIL conduct refinement, nearly 0.9 F1 scores can be obtained (in lymph node metastasis and

liver cancer samples), even without any domain expertise. One might still be tempted to answer this question in the negative, judging by the fact that about 15% of hand-drawn coarse annotations are too poor to be considered valid, and the F1 score after refinement still cannot reach 1. However, we should also be aware that most of the volunteers had no experience on digital pathology and the only "training" received was by learning from two reference samples. With slightly more standard training, the generated coarse annotations may be better and exceed the validity threshold, which then coupled with our approach could result in very accurate segmentation, but this question is out of the scope of our work. Moreover, it remains unclear what the inter- and intra-reader variability of these annotations are. Judging by other studies in different contexts [17], [18], it is natural to assume that these will also not obtain F1 scores of 1, and that a F1 scores in the range of 0.9-1 might suffice. Answering this important question remains a matter of future work.

VI. CONCLUSION

Altogether, in this paper we developed LC-MIL, a label cleaning method under a multiple instance learning framework, to automatically refine coarse annotations on a single WSI. The proposed methodology demonstrates the potential of the MIL framework in the label cleaning context, and provides a new deployment of the MIL model that can be trained on even a single slide. LC-MIL holds promise to relieve the workload of pathologists, as well as help inexperienced annotators in challenging annotation tasks.

ACKNOWLEDGMENT

The authors thank Dr. Ashley M. Cimino-Mathews and Dr. Marissa Janine White from the Department of Pathology, Johns Hopkins University, School of Medicine, for their valuable advice and insights in histopathology. The authors also kindly thank Dr. Adam Charles, Haoyang Mi and Jacopo Teneggi from the Department of Biomedical Engineering, Johns Hopkins University, for their useful advice and discussions.

REFERENCES

- [1] M. G. Hanna, A. Parwani, and S. J. Sirintrapun, "Whole slide imaging: technology and applications," *Advances in Anatomic Pathology*, vol. 27, no. 4, pp. 251–259, 2020.
- [2] R. C. Melo, M. W. Raas, C. Palazzi, V. H. Neves, K. K. Malta, and T. P. Silva, "Whole slide imaging and its applications to histopathological studies of liver disorders," *Frontiers in medicine*, vol. 6, p. 310, 2020.
- [3] J. Song, Z. Ge, X. Yang, Q. Luo, C. Wang, H. You, T. Ge, Y. Deng, H. Lin, Y. Cui *et al.*, "Hepatic stellate cells activated by acidic tumor microenvironment promote the metastasis of hepatocellular carcinoma via osteopontin," *Cancer letters*, vol. 356, no. 2, pp. 713–720, 2015.
- [4] J. A. Joyce and D. T. Fearon, "T cell exclusion, immune privilege, and the tumor microenvironment," *Science*, vol. 348, no. 6230, pp. 74–80, 2015.
- [5] H. Mi, C. Gong, J. Sulam, E. J. Fertig, A. S. Szalay, E. M. Jaffee, V. Stearns, L. A. Emens, A. M. Cimino-Mathews, and A. S. Popel, "Digital pathology analysis quantifies spatial heterogeneity of cd3, cd4, cd8, cd20, and foxp3 immune markers in triple-negative breast cancer," *Frontiers in physiology*, vol. 11, 2020.
- [6] C. Gong, R. A. Anders, Q. Zhu, J. M. Taube, B. Green, W. Cheng, I. H. Bartelink, P. Vicini, B. Wang, and A. S. Popel, "Quantitative characterization of cd8+ t cell clustering and spatial heterogeneity in solid tumors," *Frontiers in oncology*, vol. 8, p. 649, 2019.

- [7] L. O. Schwen, E. Andersson, K. Korski, N. Weiss, S. Haase, F. Gaire, H. K. Hahn, A. Homeyer, and O. Grimm, "Data-driven discovery of immune texture biomarkers," *Frontiers in oncology*, vol. 8, p. 627, 2018.
- [8] M. N. Gurcan, L. E. Boucheron, A. Can, A. Madabhushi, N. M. Rajpoot, and B. Yener, "Histopathological image analysis: A review," *IEEE reviews in biomedical engineering*, vol. 2, pp. 147–171, 2009.
- [9] S. Petushi, F. U. Garcia, M. M. Haber, C. Katsinis, and A. Toz-eren, "Large-scale computations on histology images reveal grade-differentiating parameters for breast cancer," *BMC medical imaging*, vol. 6, no. 1, pp. 1–11, 2006.
- [10] G. B. Kande, P. V. Subbaiah, and T. S. Savithri, "Unsupervised fuzzy based vessel segmentation in pathological digital fundus images," *Journal of medical systems*, vol. 34, no. 5, pp. 849–858, 2010.
- [11] M. Veta, P. J. Van Diest, R. Kornegoor, A. Huisman, M. A. Viergever, and J. P. Pluim, "Automatic nuclei segmentation in h&e stained breast cancer histopathology images," *PloS one*, vol. 8, no. 7, p. e70221, 2013.
- [12] T.-H. Song, V. Sanchez, H. Eidaly, and N. M. Rajpoot, "Dual-channel active contour model for megakaryocytic cell segmentation in bone marrow trephine histology images," *IEEE Transactions on Biomedical Engineering*, vol. 64, no. 12, pp. 2913–2923, 2017.
- [13] O. Ronneberger, P. Fischer, and T. Brox, "U-net: Convolutional networks for biomedical image segmentation," in *Proc. MICCAI*, Munich, Germany, 2015, pp. 234–241.
- [14] N. Siddique, S. Paheding, C. P. Elkin, and V. Devabhaktuni, "U-net and its variants for medical image segmentation: A review of theory and applications," *IEEE Access*, 2021.
- [15] S. Wang, D. M. Yang, R. Rong, X. Zhan, and G. Xiao, "Pathology image analysis using segmentation deep learning algorithms," *The American journal of pathology*, vol. 189, no. 9, pp. 1686–1698, 2019.
- [16] T. A. Longacre, M. Ennis, L. A. Quenneville, A. L. Bane, I. J. Bleiweiss, B. A. Carter, E. Catelano, M. R. Hendrickson, H. Hibshoosh, L. J. Layfield *et al.*, "Interobserver agreement and reproducibility in classification of invasive breast carcinoma: an nci breast cancer family registry study," *Modern pathology*, vol. 19, no. 2, pp. 195–207, 2006.
- [17] F. A. Foss, S. Milkins, and A. H. McGregor, "Inter-observer variability in the histological assessment of colorectal polyps detected through the nhs bowel cancer screening programme," *Histopathology*, vol. 61, no. 1, pp. 47–52, 2012.
- [18] L. C. Van Den Einden, J. A. De Hullu, L. F. Massuger, J. M. Grefte, P. Bult, A. Wiersma, A. C. Van Engen-van Grunsven, B. Sturm, S. L. Bosch, H. Hollema *et al.*, "Interobserver variability and the effect of education in the histopathological diagnosis of differentiated vulvar intraepithelial neoplasia," *Modern pathology*, vol. 26, no. 6, pp. 874–880, 2013.
- [19] V. Cheplygina, M. de Bruijne, and J. P. Pluim, "Not-so-supervised: a survey of semi-supervised, multi-instance, and transfer learning in medical image analysis," *Medical image analysis*, vol. 54, pp. 280–296, 2019.
- [20] G. Campanella, M. G. Hanna, L. Geneslaw, A. Miraffior, V. W. K. Silva, K. J. Busam, E. Brogi, V. E. Reuter, D. S. Klimstra, and T. J. Fuchs, "Clinical-grade computational pathology using weakly supervised deep learning on whole slide images," *Nature medicine*, vol. 25, no. 8, pp. 1301–1309, 2019.
- [21] M. Y. Lu, D. F. Williamson, T. Y. Chen, R. J. Chen, M. Barbieri, and F. Mahmood, "Data-efficient and weakly supervised computational pathology on whole-slide images," *Nature Biomedical Engineering*, vol. 5, no. 6, pp. 555–570, 2021.
- [22] C. L. Srinidhi, O. Ciga, and A. L. Martel, "Deep neural network models for computational histopathology: A survey," *Medical Image Analysis*, p. 101813, 2020.
- [23] H.-T. Cheng, C.-F. Yeh, P.-C. Kuo, A. Wei, K.-C. Liu, M.-C. Ko, K.-H. Chao, Y.-C. Peng, and T.-L. Liu, "Self-similarity student for partial label histopathology image segmentation," in *Proc. ECCV*, Glasgow, UK, 2020, pp. 117–132.
- [24] S. Sukhbaatar, J. Bruna, M. Paluri, L. Bourdev, and R. Fergus, "Training convolutional networks with noisy labels," *arXiv preprint arXiv:1406.2080*, 2014.
- [25] J. Goldberger and E. Ben-Reuven, "Training deep neural-networks using a noise adaptation layer," in *Proc. ICLR*, Toulon, France, 2017.
- [26] Y. Dgani, H. Greenspan, and J. Goldberger, "Training a neural network based on unreliable human annotation of medical images," in *Proc. ISBI*, Washington, DC, USA, 2018, pp. 39–42.
- [27] A. Ghosh, H. Kumar, and P. Sastry, "Robust loss functions under label noise for deep neural networks," in *Proc. AAAI Conference on Artificial Intelligence*, vol. 31, no. 1, San Francisco, CA, USA, 2017.
- [28] D. J. Matuszewski and I.-M. Sintorn, "Minimal annotation training for segmentation of microscopy images," in *Proc. ISBI*, Washington, DC, USA, 2018, pp. 387–390.
- [29] B. Rister, D. Yi, K. Shivakumar, T. Nobashi, and D. L. Rubin, "Ct organ segmentation using gpu data augmentation, unsupervised labels and iou loss," *arXiv preprint arXiv:1811.11226*, 2018.
- [30] B.-B. Gao, C. Xing, C.-W. Xie, J. Wu, and X. Geng, "Deep label distribution learning with label ambiguity," *IEEE Transactions on Image Processing*, vol. 26, no. 6, pp. 2825–2838, 2017.
- [31] H. H. Pham, T. T. Le, D. Q. Tran, D. T. Ngo, and H. Q. Nguyen, "Interpreting chest x-rays via cnns that exploit hierarchical disease dependencies and uncertainty labels," *Neurocomputing*, vol. 437, pp. 186–194, 2021.
- [32] M. Islam and B. Glocker, "Spatially varying label smoothing: Capturing uncertainty from expert annotations," in *Proc. IPMI*, 2021, pp. 677–688.
- [33] C. G. Northcutt, T. Wu, and I. L. Chuang, "Learning with confident examples: Rank pruning for robust classification with noisy labels," in *Proc. UAI*, Sydney, Australia, 2017, pp. 1321–1330.
- [34] Y. Ding, L. Wang, D. Fan, and B. Gong, "A semi-supervised two-stage approach to learning from noisy labels," in *Proc. WACV*, Lake Tahoe, NV, USA, 2018, pp. 1215–1224.
- [35] J. M. Köhler, M. Autenrieth, and W. H. Beluch, "Uncertainty based detection and relabeling of noisy image labels." Presented at CVPR Workshops, 2019.
- [36] X. Wang, Y. Hua, E. Kodirov, and N. Robertson, "Emphasis regularisation by gradient rescaling for training deep neural networks with noisy labels," *arXiv*, 2019.
- [37] J. Shu, Q. Xie, L. Yi, Q. Zhao, S. Zhou, Z. Xu, and D. Meng, "Meta-weight-net: Learning an explicit mapping for sample weighting," in *Proc. NeurIPS*, Vancouver, British Columbia, 2019, pp. 1917–1928.
- [38] C. Guo, G. Pleiss, Y. Sun, and K. Q. Weinberger, "On calibration of modern neural networks," in *Proc. ICML*, Sydney, Australia, 2017, pp. 1321–1330.
- [39] P. D. Vo, A. Ginsca, H. Le Borgne, and A. Popescu, "Effective training of convolutional networks using noisy web images," in *Proc. CBMI*, Prague, Czech, 2015, pp. 1–6.
- [40] K.-H. Lee, X. He, L. Zhang, and L. Yang, "Cleannet: Transfer learning for scalable image classifier training with label noise," in *Proc. CVPR*, Salt Lake City, Utah, 2018, pp. 5447–5456.
- [41] M. Ren, W. Zeng, B. Yang, and R. Urtasun, "Learning to reweight examples for robust deep learning," in *Proc. ICML*, Stockholm, Sweden, 2018, pp. 4334–4343.
- [42] H. Le, D. Samaras, T. Kurc, R. Gupta, K. Shroyer, and J. Saltz, "Pancreatic cancer detection in whole slide images using noisy label annotations," in *Proc. MICCAI*, Shenzhen, China, 2019, pp. 541–549.
- [43] Z. Mirikharaji, Y. Yan, and G. Hamarneh, "Learning to segment skin lesions from noisy annotations," in *Domain Adaptation and Representation Transfer and Medical Image Learning with Less Labels and Imperfect Data*. Springer, 2019, pp. 207–215.
- [44] D. L. Wilson, "Asymptotic properties of nearest neighbor rules using edited data," *IEEE Transactions on Systems, Man and Cybernetics*, vol. 2, 1972.
- [45] D. Bahri, H. Jiang, and M. Gupta, "Deep k-nn for noisy labels," in *Proc. ICML*, 2020, pp. 540–550.
- [46] T. G. Dietterich, R. H. Lathrop, and T. Lozano-Pérez, "Solving the multiple instance problem with axis-parallel rectangles," *Artificial Intelligence*, vol. 89, no. 1, pp. 31–71, 1997.
- [47] M. Ilse, J. Tomczak, and M. Welling, "Attention-based deep multiple instance learning," in *Proc. ICML*, Stockholm, Sweden, 2018, pp. 2127–2136.
- [48] Y. Xu, J.-Y. Zhu, I. Eric, C. Chang, M. Lai, and Z. Tu, "Weakly supervised histopathology cancer image segmentation and classification," *Medical image analysis*, vol. 18, no. 3, pp. 591–604, 2014.
- [49] P. Courtiol, E. W. Tramel, M. Sanselme, and G. Wainrib, "Classification and disease localization in histopathology using only global labels: A weakly-supervised approach," *arXiv preprint arXiv:1802.02212*, 2018.
- [50] X. Wang, Y. Yan, P. Tang, X. Bai, and W. Liu, "Revisiting multiple instance neural networks," *Pattern Recognition*, vol. 74, pp. 15–24, 2018.
- [51] Z. Jia, X. Huang, I. Eric, C. Chang, and Y. Xu, "Constrained deep weak supervision for histopathology image segmentation," *IEEE transactions on medical imaging*, vol. 36, no. 11, pp. 2376–2388, 2017.
- [52] G. Xu, Z. Song, Z. Sun, C. Ku, Z. Yang, C. Liu, S. Wang, J. Ma, and W. Xu, "Camel: A weakly supervised learning framework for histopathology image segmentation," in *Proc. ICCV*, Seoul, Korea, 2019, pp. 10 682–10 691.

- [53] J. Mukhoti, V. Kulharia, A. Sanyal, S. Golodetz, P. H. Torr, and P. K. Dokania, "Calibrating deep neural networks using focal loss," *arXiv preprint arXiv:2002.09437*, 2020.
- [54] G. Litjens, P. Bandi, B. E. Bejnordi, O. Geessink, M. Balkenhol, P. Bult, A. Halilovic, M. Hermesen, R. van de Loo, R. Vogels, Q. F. Manson, N. Stathonikos, A. Baidoshvili, P. van Diest, C. Wauters, M. van Dijk, and J. van der Laak, "1399 h&e-stained sentinel lymph node sections of breast cancer patients: The camelyon dataset," *GigaScience*, vol. 7, 2018.
- [55] Y. J. Kim, H. Jang, K. Lee, S. Park, S.-G. Min, C. Hong, J. H. Park, K. Lee, J. Kim, W. Hong *et al.*, "Paip 2019: Liver cancer segmentation challenge," *Medical Image Analysis*, vol. 67, p. 101854, 2021.
- [56] F. Wilcoxon, "Individual comparisons by ranking methods," *Biometrics Bulletin*, vol. 1, no. 6, pp. 80–83, 1945.
- [57] N. Otsu, "A threshold selection method from gray-level histograms," *IEEE Transactions on Systems, Man, and Cybernetics*, vol. 9, no. 1, pp. 62–66, 1979.
- [58] K. Simonyan and A. Zisserman, "Very deep convolutional networks for large-scale image recognition," in *Proc. ICLR*, San Diego, CA, USA, 2015.
- [59] J. Deng, W. Dong, R. Socher, L.-J. Li, K. Li, and L. Fei-Fei, "Imagenet: A large-scale hierarchical image database," in *Proc. CVPR*, Miami, FL, USA, 2009, pp. 248–255.
- [60] D. P. Kingma and J. L. Ba, "Adam: A method for stochastic optimization," in *Proc. ICLR*, San Diego, CA, USA, 2015.

Supplementary Material

I. IMPLEMENTATION DETAILS

Tissue region identification: For each digitized slide, our pipeline begins with the automatic detection of tissue regions to exclude irrelevant (e.g. blank) sections. Gigapixel WSIs are first loaded into memory at a downsampled resolution (e.g., $256\times$ downscale), and then image processing approaches are applied to the down-sampled thumbnails. The detection methods vary slightly for different data source. For CAMELYON16, the downsampled thumbnail is converted from RGB color space to the HSV color space. The Otsu algorithm [57] is applied to H and S channels independently and then two masks are combined (employing logic AND) to generate the final binary mask. For PAIP2019 and PAIP2020, the tissue mask is generated by applying the RGB thresholds (235, 210, 235) on images, as suggested by the data provider.

Patch extraction: The size of patch is set to 256×256 (pixels). Technically, every pixel can be the center of a unique patch, resulting in millions of patches that highly overlap with each other. In this way, the predicted heatmaps or lesion maps have the same size and resolution as the original WSIs. However, such an approach is extremely computationally intensive and time consuming, turning it prohibitive. In our experiments, we extracted patches with no overlap in WSIs scanned at $\times 40$ magnification (CAMELYON16 and PAIP2020). For slides scanned at $\times 20$ magnification (PAIP2019), cropped patches have 75% overlap with neighborhood patches. The size and overlapping of cropped patches can impact the resolution of predicted heatmaps. For CAMELYON16 and PAIP2020, the predicted heatmap is $256\times$ downsampled of the original WSI; for PAIP2019, the predicted heatmap is $128\times$ downsampled of the original WSI. Our overall approach is not limited to these choices, and could be applicable to other settings too.

Generation of simulated coarse annotations: The procedure can be described by the following three steps: (1) Retain only the largest cancerous region and omit all the others; (2) Performing the morphological operation of dilation to the remaining cancerous region; (3) Create the convex hull for the dilated lesion. As a particular case, since almost all of the WSIs in PAIP2020 contain only one cancerous region, the only cancerous region was cut in half.

Neural networks architecture: Both feature extractors used in DkNN (f_{ψ_1}) and in LC-MIL (f_{ψ_2}) are built based on the 16-layer VGGNet architecture [58]. The last FCN layer is removed to generate f_{ψ_1} , while f_{ψ_2} uses the original 16-layer VGGNet architecture. Since the training data is limited (one WSI), the VGGNet used has been pre-trained on the ImageNet dataset [59]. When they are further fine-tuned on the histopathology images, the parameters in the convolutional layers are kept constant.

Learning hyper-parameters: The binary classifier \mathbb{C} used in DkNN is trained on patches in a fully supervised manner. Adam optimizer [60] is used with a learning rate of 5×10^{-5} . Since the number of patches is substantially large, all patches

are iterated only once during training. The MIL model used in LC-MIL is trained on 1,000 MIL bags, consisting of 500 positive bags and 500 negative bags. Adam optimizer is used with an initial learning rate of 5×10^{-5} , and the learning rate decays to 50% for every 100 bags.

Post-processing: To obtain a fair comparison between the annotations before and after refinement, we conduct some simple post-processing on the heatmaps generated by either DkNN (binary map) or LC-MIL (scalar map). The binary heatmap predicted by DkNN is post-processed by simple morphology operations: both small holes (smaller than 100 pixels) and small objects (smaller than 100 pixels) are removed. The scalar heatmap predicted by LC-MIL is first converted to a binary map by: (1) smoothing it using a 3×3 Gaussian kernel with a standard deviation $\sigma = 1$; (2) applying a threshold $v_0 = 0.6$, and then applying the same morphology operations conducted for DkNN.

Other user-specified parameters:

- 1) Number of nearest neighbors k in DkNN algorithm: We set k as 5 in the experiments. It should also be noted that DkNN algorithm is not sensitive to the setting of k , and the setting of 3, 5, 7 will all get very similar results.
- 2) Length of bag n_j in the LC-MIL algorithm: We use a binomial distribution for n_j , so that $n_j \sim \mathbb{B}(20, 0.5)$.
- 3) Parameter γ in the focal loss function: We set the parameter γ as suggested by [53]. That is $\gamma = 5$ for $P(Y_j = 1) \in [0, 0.2)$, and $\gamma = 3$ for $P(Y_j = 1) \in [0.2, 1]$.

II. SUPPLEMENTARY FIGURES

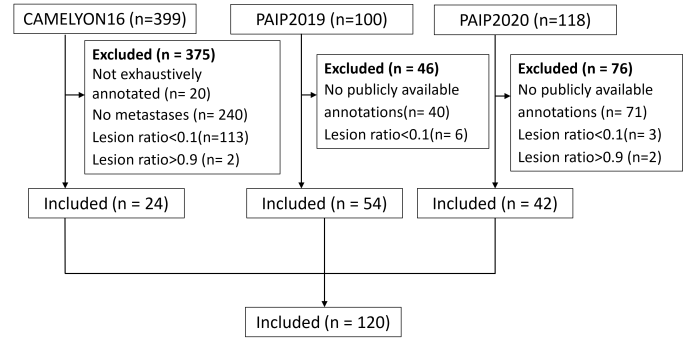


Fig. 1: **Data inclusion diagram.** A total of 120 slides are included. 24 of them are lymph node sections from breast cancer patients (CAMELYON16), 54 of them are liver cancer resection samples (PAIP2019), and the other 42 are colorectal cancer resection samples (PAIP2020).

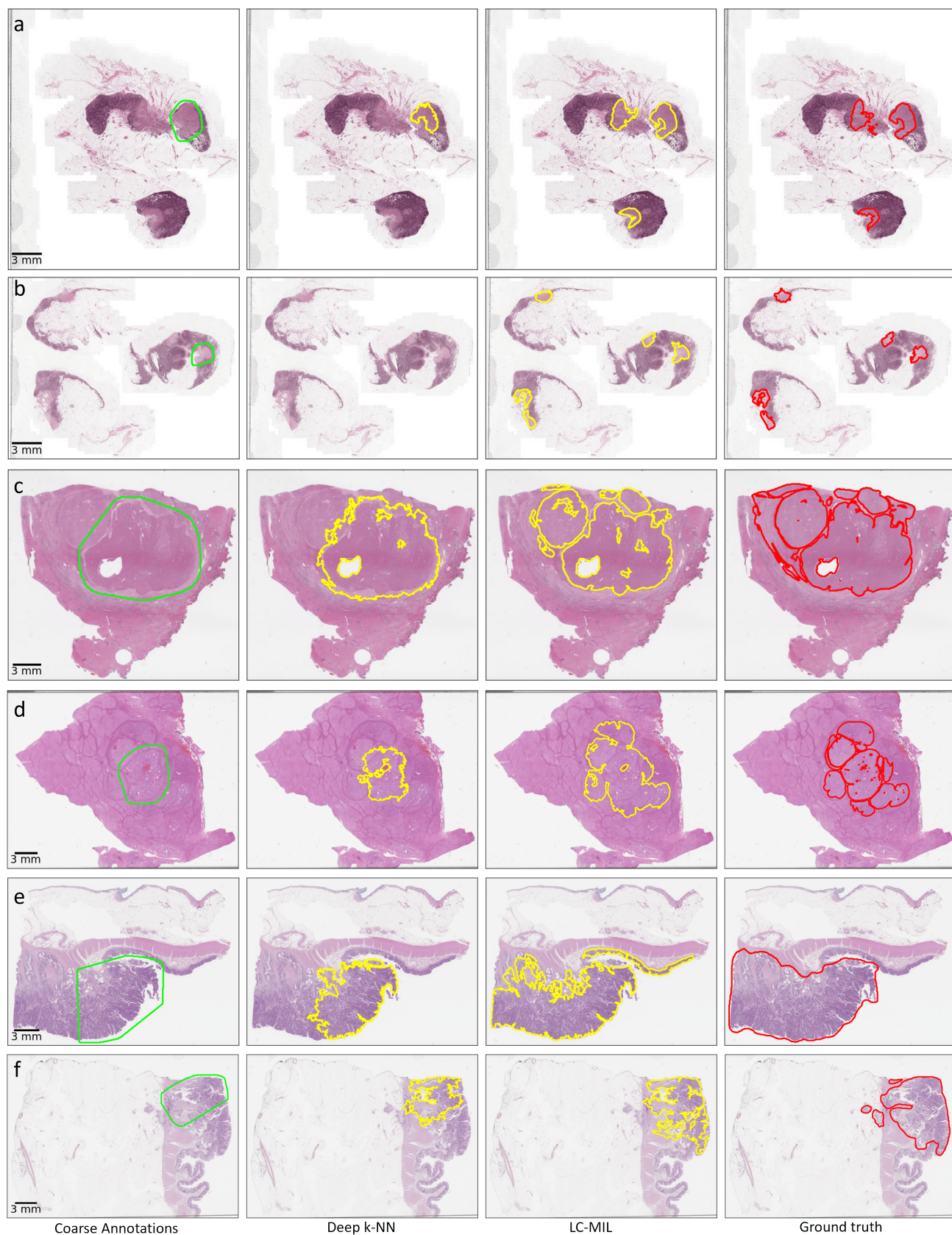


Fig. 2: **Supplementary examples of simulated coarse annotations and refinement.** (a)-(b): two examples from CAME-LYON16; (c)-(d): two examples from PAIP2019; (e)-(f) two examples from PAIP2020.

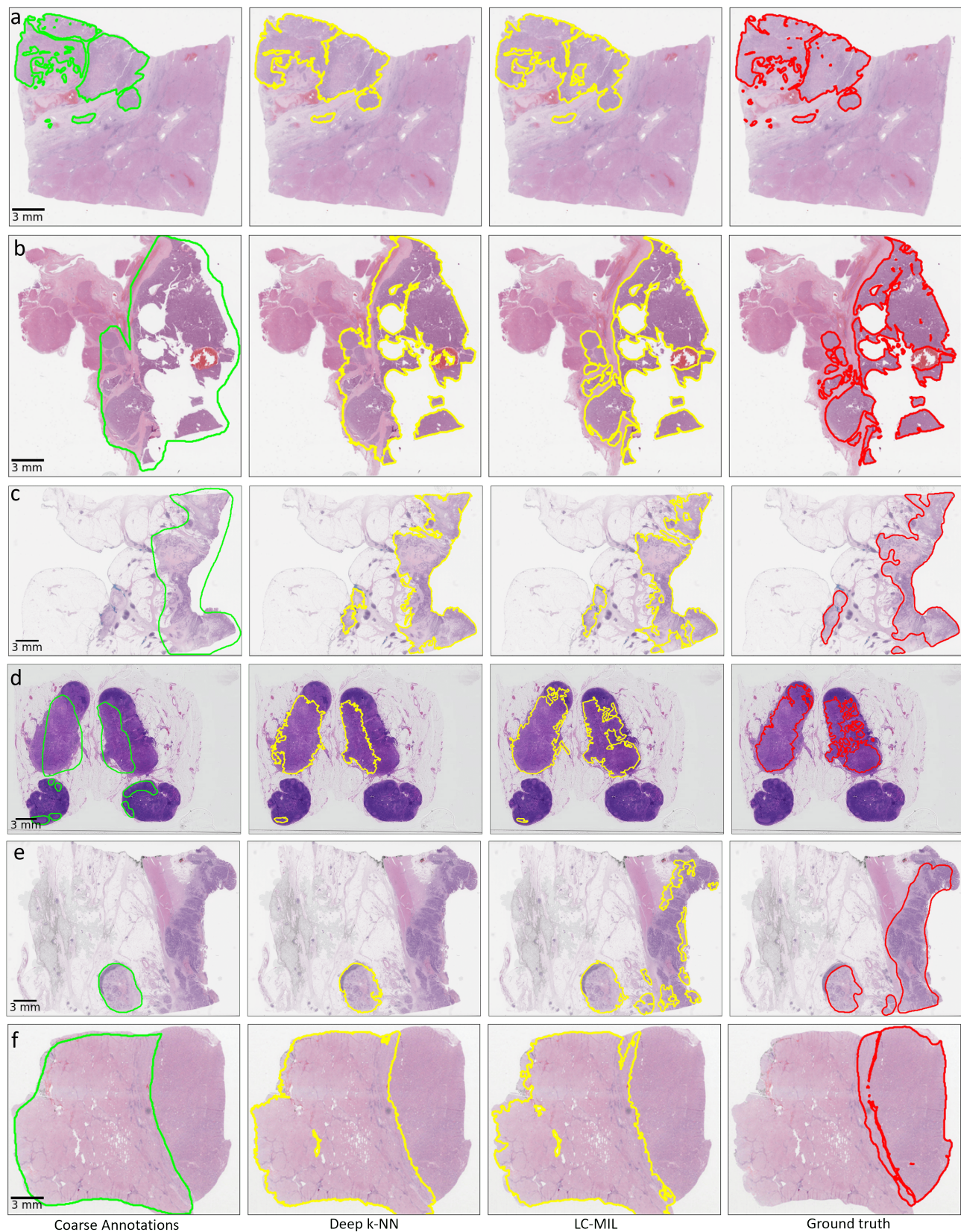


Fig. 3: Examples of hand-drawn coarse annotations and refinement. (a) correct lesion detection and precise boundaries; (b)-(d): roughly correct annotations with small imperfection, including rough boundaries (b), a few missed lesions (c), and some false positive detection (d); (e)-(f) incorrect annotations, including main lesion missed (e), and flipped labels (f).

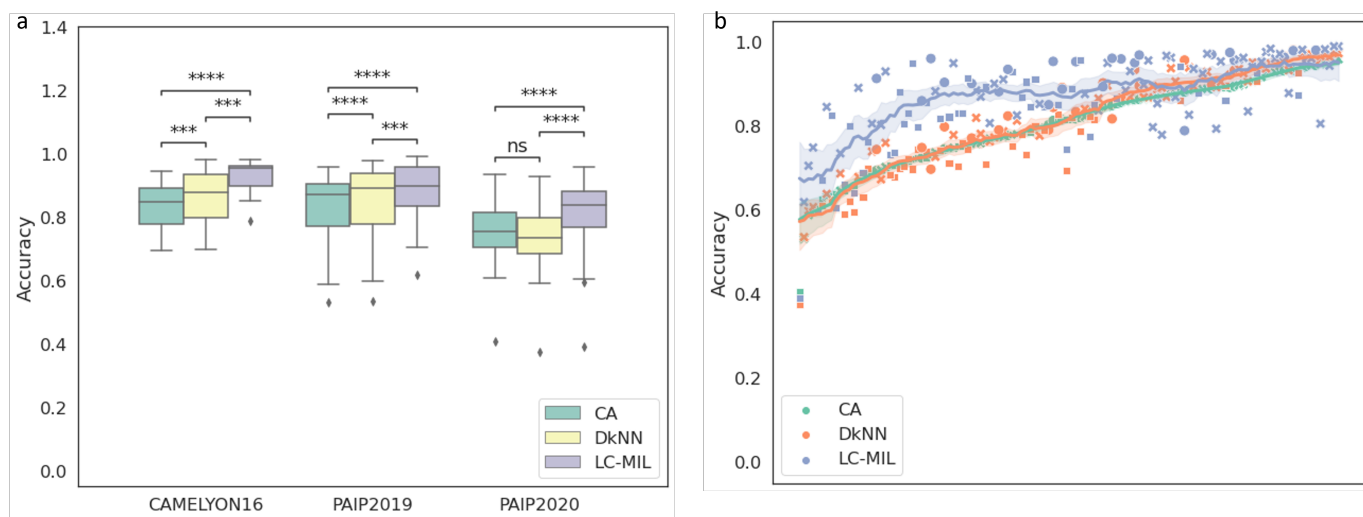


Fig. 4: **Overview of refinement on simulated coarse annotations (accuracy).** (a) Boxplots of accuracy of three versions of annotations. (b) Refinement performance (accuracy) in different label noise conditions, slides sorted by the accuracy of coarse annotations.